Cell Reports
Methods

Article

Sparse imaging and reconstruction tomography for high-speed high-resolution whole-brain imaging

Graphical abstract

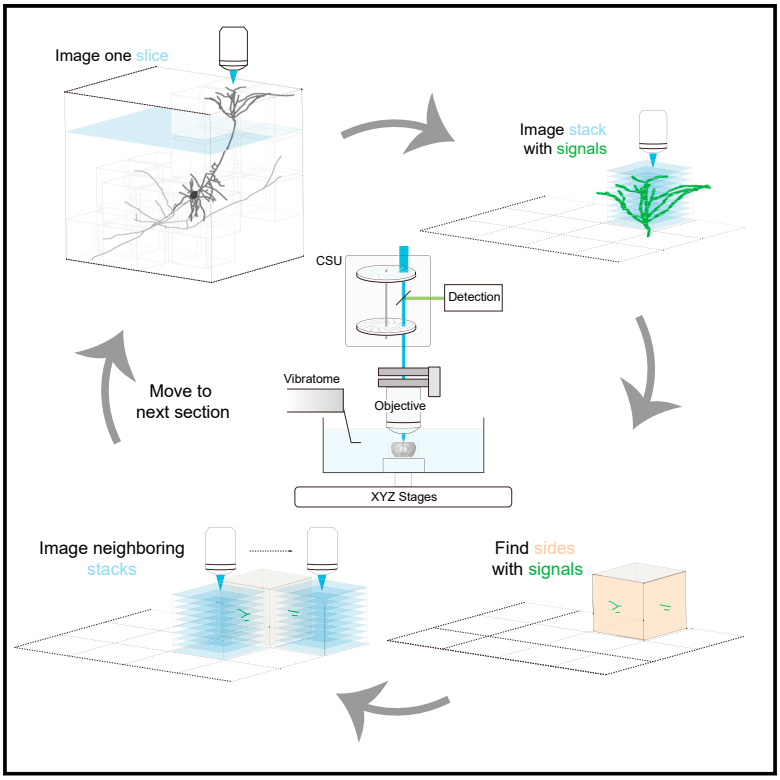

Highlights

- A sparse imaging and reconstruction tomography (SMART) system for whole-brain imaging
- Initial signal detection prioritizes imaging of sparsely labeled neurons
- SMART enables brain-wide imaging at synaptic resolution in about 20 h
- Prefrontal, premotor, and visual neurons have distinct morphological features

Authors

Han Chen, Tianyi Huang, Yuexin Yang, ..., Runan Ji, Hongjiang Yang, Zengcai V. Guo

Correspondence

guozengcai@tsinghua.edu.cn

In brief

Brain-wide imaging at synaptic resolution presents a huge challenge in data acquisition and processing. Here, Chen et al. develop sparse imaging and reconstruction tomography (SMART), which enables high-speed high-resolution whole-brain imaging to facilitate single-neuron reconstruction.

Chen et al., 2021, Cell Reports Methods *1*, 100089
October 25, 2021
https://doi.org/10.1016/j.crmeth.2021.100089

CellPress

Cell Reports Methods

CellPress
OPEN ACCESS

Article

Sparse imaging and reconstruction tomography for high-speed high-resolution whole-brain imaging

Han Chen,[1,3,4] Tianyi Huang,[1,3,4] Yuexin Yang,[1,3,4] Xiao Yao,[2,3] Yan Huo,[1,3] Yu Wang,[2,3] Wenyu Zhao,[2,3] Runan Ji,[1,3] Hongjiang Yang,[1,3] and Zengcai V. Guo[1,2,3,5,*]

[1]School of Medicine, Tsinghua University, Beijing 100084, China
[2]Tsinghua-Peking Joint Center for Life Sciences, Beijing 100084, China
[3]IDG/McGovern Institute for Brain Research, Tsinghua University, Beijing 100084, China
[4]These authors contributed equally
[5]Lead contact
*Correspondence: guozengcai@tsinghua.edu.cn
https://doi.org/10.1016/j.crmeth.2021.100089

MOTIVATION Different brain areas communicate in order to produce a given behavior. Understanding brain function therefore requires detailed knowledge of how information flows through long-range neural circuits. Illuminating long-range structures requires whole-brain imaging at high resolution to trace axonal arbors of individual neurons to their termini across the brain; however, current platforms are complicated and require 1–2 weeks of continuous imaging for each mouse brain. To address this challenge, we have developed an imaging strategy that enables high-speed, high-resolution, high-contrast brain-wide imaging to reconstruct sparsely labeled neurons in their entirety.

SUMMARY

Understanding brain functions requires detailed knowledge of long-range connectivity through which different areas communicate. A key step toward illuminating the long-range structures is to image the whole brain at synaptic resolution to trace axonal arbors of individual neurons to their termini. However, high-resolution brain-wide imaging requires continuous imaging for many days to sample over 10 trillion voxels, even in the mouse brain. Here, we have developed a sparse imaging and reconstruction tomography (SMART) system that allows brain-wide imaging of cortical projection neurons at synaptic resolution in about 20 h, an order of magnitude faster than previous methods. Analyses of morphological features reveal that single cortical neurons show remarkable diversity in local and long-range projections, with prefrontal, premotor, and visual neurons having distinct distribution of dendritic and axonal features. The fast imaging system and diverse projection patterns of individual neurons highlight the importance of high-resolution brain-wide imaging in revealing full neuronal morphology.

INTRODUCTION

The mammalian brain consists of several hundred functionally distinct regions that form complex networks through their dense inter-areal connections (Felleman and Van Essen, 1991; Glasser et al., 2016; Oh et al., 2014). These long-range connections direct how information flows across brain regions, and thus play a crucial role in sensory processing, perception, working memory, decision-making, and execution of actions (Alexander et al., 1990; Glickfeld et al., 2013; Guo et al., 2017; Otis et al., 2017). Great efforts have been devoted to probe brain-wide inter-areal connectivity using techniques with varied spatial scales. Functional imaging methods provide coarse spatial organization, as they typically sample mammalian brains at the millimeter scale (Heeger and Ress, 2002). Bulk application of anterograde and retrograde tracers followed by light microscopy can achieve micrometer-scale resolution, but they average over a large population of neurons and obscure fine projection patterns of individual neurons (Gerfen and Sawchenko, 1984; Luppi et al., 1990; Oh et al., 2014; Veenman et al., 1992; Zingg et al., 2014), as neurons in one brain area are typically composed of subpopulations with distinct projection targets to mediate distinct functions. Full morphological reconstructions can reveal individual neurons' complicated projection patterns, which are often widely diverse but arranged in an intermingled way with neighboring neurons (Wang et al., 2019b; Winnubst et al., 2019). Morphological properties of axonal and dendritic arbors provide crucial information to classify cell types (Sanes and Masland, 2015), and strongly influence the firing properties and computational capabilities of individual neurons

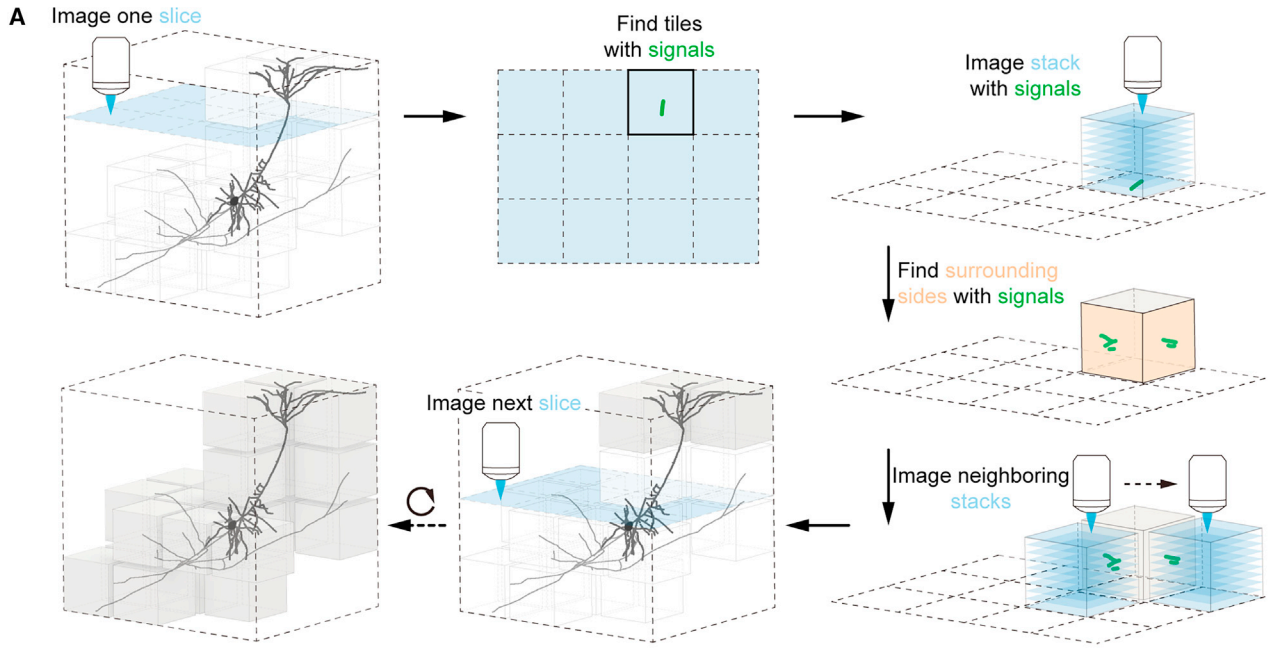

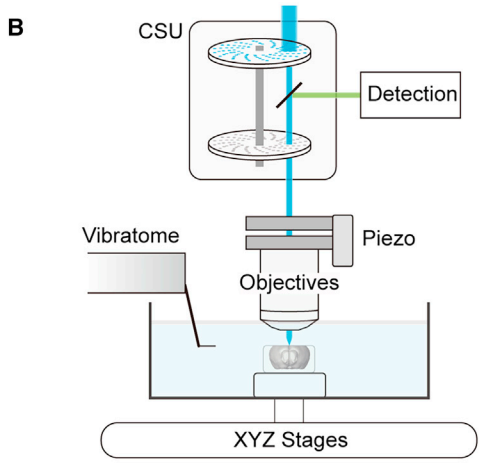

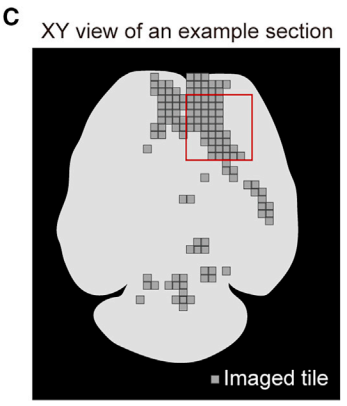

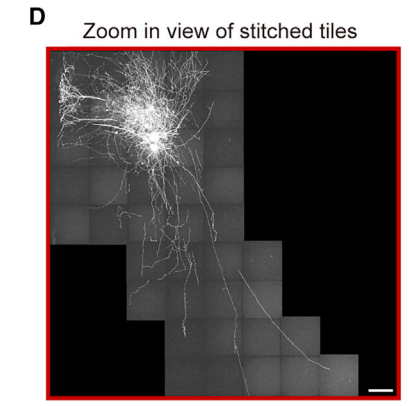

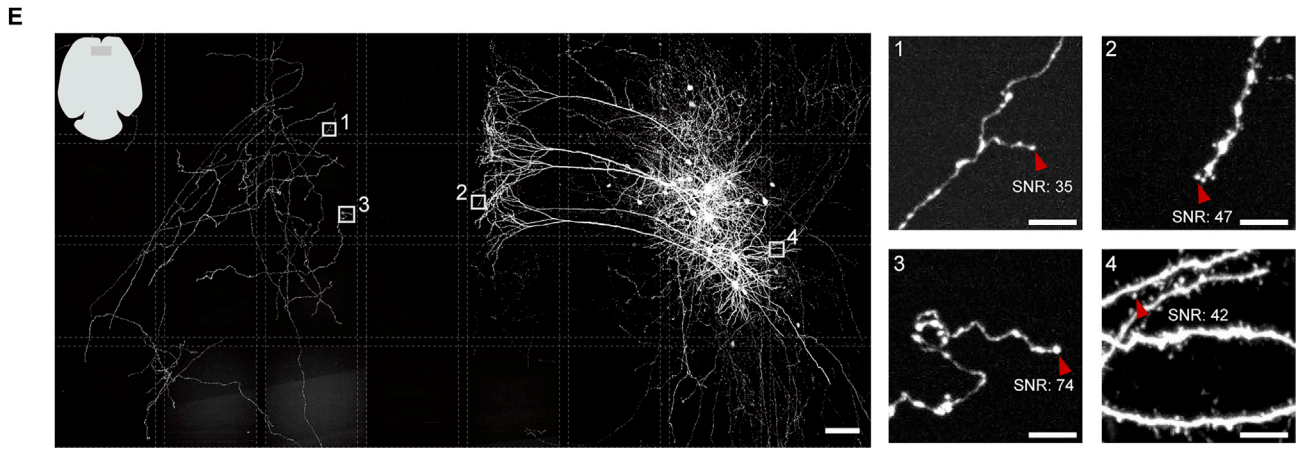

(legend on next page)

(Mainen and Sejnowski, 1996). However, despite the importance of obtaining full neuronal morphology, complete reconstruction is still technically challenging, as it requires high-contrast brain-wide scanning at sub-micrometer resolution and is achieved only in scattered cases that typically require specialized imaging systems and prolonged imaging time (Economo et al., 2016; Ghosh et al., 2011; Gong et al., 2016; Han et al., 2018; Kuramoto et al., 2009; Li et al., 2010; Wang et al., 2019b; Winnubst et al., 2019; Wu et al., 2014).

Specialized imaging platforms and their associated reconstruction pipelines have been developed to detect and trace full neuronal morphology. Micro-optical sectioning tomography (MOST) can scan a whole mouse brain at ~0.3 × 0.3 × 1 μm^3 voxel in 8 days, and an updated version of wide-field large-volume tomography (WVT) can image at a reduced voxel size of 0.32 × 0.32 × 2 μm^3 in 3 days (Gong et al., 2016; Li et al., 2010). Serial two-photon tomography integrates laser-scanning two-photon microscopy with vibratome-based tissue sectioning to image one mouse brain at 0.3 × 0.3 × 1 μm^3 voxel in 7 days (Economo et al., 2016). The long duration of imaging and the large dataset collected (~10–20 TB) pose a huge challenge for imaging and data processing. Light-sheet fluorescence microscopy combined with tissue clearing techniques, and spinning-disk confocal or two-photon systems integrated with a vibratome for serial sectioning, have achieved volumetric imaging of mouse brains in a few hours but at reduced resolution (especially along the z axis) (Dodt et al., 2007; Migliori et al., 2018; Narasimhan et al., 2017; Ragan et al., 2012; Seiriki et al., 2017; Wang et al., 2019a). Thus, few techniques can image a whole mouse brain at synaptic resolution within a relatively short time (approximately a day) to enable efficient reconstruction of complete neuronal morphology. Here, we have developed a high-speed high-resolution serial-sectioning imaging system, which acquired a whole mouse brain with sparsely labeled neurons in its entirety in about 20 h (the exact time depends on the projection complexity of labeled neurons in one or several cortical areas, Figure 1).

RESULTS

Working principles and setup

Sparse but strong labeling facilitates the disentanglement of single neuronal fibers from the surrounding dendritic and axonal processes, and thus is a fundamental requirement for reconstruction of full neuronal morphology using light microscopy (Economo et al., 2016; Lin et al., 2018; Winnubst et al., 2019). A robust sparse labeling method is to inject a mixture of high-titer EGFP virus and low-titer Cre virus (Xu et al., 2012). This approach can randomly label a few dozens of neurons near the injection site to allow visualization of individual spines *in vivo* (Xu et al., 2012) and to allow detection and reconstruction of long-range projections in cleared brains (Economo et al., 2016; Winnubst et al., 2019). We posited that sparse signal introduced through viral injection extends along only the labeled neuronal structures, and this feature can be used to speed up imaging. To fully exploit the sparsity of signals, we aim to image only regions with fluorescent signals (Figure 1A). At first sight, this is paradoxical: how do we know which region has a fluorescent signal without imaging the region first? We achieve this based on the fact that axonal and dendritic arbors emanating from a soma are continuous, and a projection neuron with its full process cannot be fitted into a small cuboid with each dimension spanning a few hundred micrometers. Thus, if there is no fluorescent signal on the surface of a cuboid, there would be no signal within the cuboid. During the process of imaging, we determine whether there exists signal on the surface in order to avoid imaging empty cuboids. We use this approach to speed up data acquisition and reconstruction (i.e., sparse imaging and reconstruction tomography, SMART).

With this concept, we built an imaging system based on a spinning-disk confocal system equipped with a 40× oil objective (NA 1.3) and a high-quantum-yield back-illuminated scientific complementary-metal-oxide semiconductor (sCMOS) camera (11 × 11 μm^2 pixel size), which provides high-resolution imaging (0.3 × 0.3 × 1.0 μm^3 voxel, Figures 1B, 1E, and S1). Alternatively, we optimized the system with a long-working-distance objective (25×, NA 1.0) to achieve faster imaging (~2× due to a larger field of view) at slightly reduced resolution (0.4 × 0.4 × 1.0 μm^3 voxel size, high-speed setup, see STAR Methods for details). Tissue clearing with CUBIC-1 (Susaki et al., 2014) combined with OPTIClear (Susaki et al., 2014) for refractive index matching allows the spinning-disk confocal unit to image 250 μm thick slices without evident signal degradation (Figure S2B). A vibratome is integrated to section off the imaged top portion of tissue (~195 μm) to achieve constant quality of imaging throughout

Figure 1. SMART system enables high-speed high-resolution whole-brain imaging

(A) Schematic of imaging strategy to detect regions with fluorescent signals. Imaging a brain is decomposed into imaging all the cuboids within the brain volume. As a single neuron is structurally continuous, its extensive dendrites and axon arbors cannot be fitted into a cuboid with each dimension spanning a few hundred micrometers. Thus, a cuboid is empty of fluorescent signal if there is no fluorescent signal on its six surfaces. In contrast, if a cuboid has signal on any surface, there are fluorescent signals within the cuboid (or on its surfaces) and the cuboid should be imaged.

(B) The system setup. Shown are a confocal spinning-disk unit (CSU), objectives, a vibratome for serial sectioning, and x-y-z stages for positioning a cleared mouse brain.

(C) An example section with imaged tiles indicated in dark gray.

(D) Zoom-in view of the stitched tiles in (C) showing a portion of the dendrites and axons from a few dozens of labeled medial prefrontal cortex (mPFC) neurons. Scale bar: 200 μm.

(E) Left: maximum-intensity projection of a large volume (1.5 × 2.4 × 0.6 mm^3) consisting of 120 tiles from the same brain in (C). Labeled somata and neurites are depicted in the x-y view (left). Scale bar: 100 μm. Right: zoom-in views of rectangular regions on the left show axon branchpoints, axon terminals, dendrites, and dendritic ends. SNR, signal-to-noise ratio of structures indicated by arrowheads. Scale bars: 10 μm.

See also Figures S1 and S2.

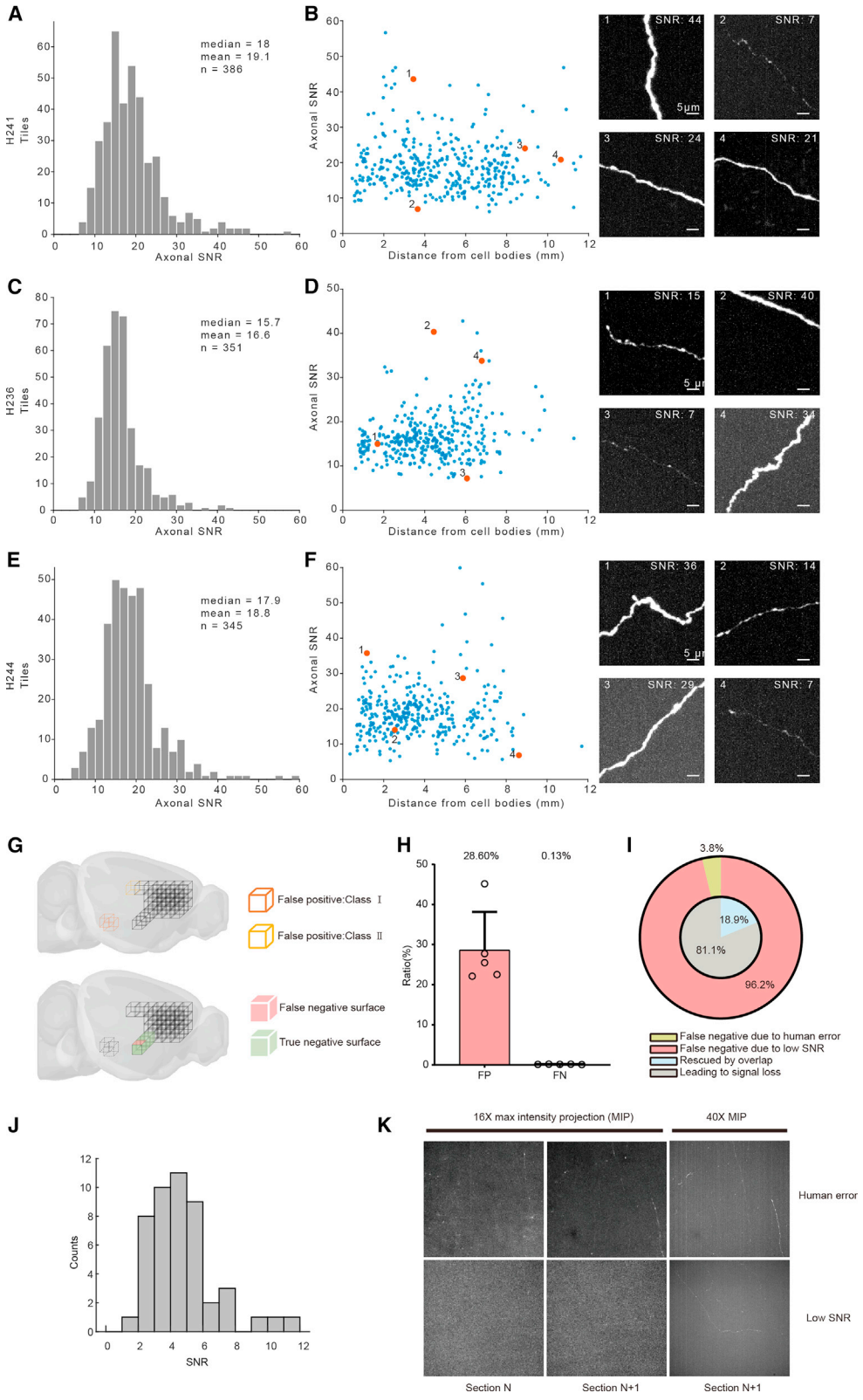

(legend on next page)

the cleared mouse brain (Figure S1). As the system uses a high NA objective, fine structures such as spines and thin axons are imaged with high signal-over-noise ratio (SNR), and there is no evident degradation of the SNR with increased distance from somata (Figures 1E and 2A–2F). Axons and their terminals have a high SNR and are clearly visible (Figure 3).

The strategy of sparse imaging crucially depends on successful detection of signals on the surfaces of each cuboid. To quantify the accuracy of signal detection, we calculated the false positive and false negative rates in multiple imaged brain samples (STAR Methods). False positive rate, defined as the fraction of imaged tiles without fluorescent signals, reached 28.6% on average (Figure 2H). These extra tiles prolonged imaging time roughly by the same percentage. False negative rate was limited to 0.13%, equivalent to approximately nine surfaces in imaged brain samples (with about 7,000 surfaces surrounding imaged stacks). We also imaged cleared brains completely using the high-speed setup, and the false negative rate was about 0.65%. The undetected surfaces are typically due to faint axons from weakly labeled neurons, as the viral delivery strategy does not label neurons with uniform brightness (accounting for over 96% of cases, Figure 2I). We characterized the brightness of signals on false negatively detected surfaces (Figure 2J). The signals on these surfaces have low SNR of 4.6 ± 2.1 (mean ± SD, n = 47). Low-fluorescence signals render tracing the full neuronal morphology almost impossible, and thus, the undetected signals on surfaces do not affect our pipeline of brain-wide imaging and reconstruction.

Physical sectioning and other factors such as temperature fluctuations can lead to tissue deformation. We characterized the deformation field and found that mismatches between adjacent sections were at 10 μm scale along the x, y, and z directions (Figures S2F and S2G). As stacks of images are acquired with partially overlapped regions in all dimensions (10% or ∼30 μm in the x and y directions, 55 μm along the z direction), we used Elastix (Klein et al., 2010) to register adjacent regions (Figures S2H–S2J). A zoom-in view of a stitched volume comprising 120 stacks (1.5 × 2.4 × 0.6 mm^3) reveals distal axon collaterals in the contralateral hemisphere with high contrast and natural continuity (Figure 1E).

Imaging prefrontal, premotor, and visual cortical neurons

Cortical projection neurons have distinct cell types with different innervation targets (Harris and Shepherd, 2015; Oh et al., 2014; Wang et al., 2019b; Winnubst et al., 2019). We used SMART to image sparsely labeled EGFP neurons in the medial prefrontal cortex (mPFC; a frontal region in the regulation of cognitive and emotive functions; Fuster, 2015; Miller, 2000), the anterior lateral motor cortex (ALM; a premotor region in the regulation of motor planning and movement; Guo et al., 2014; Li et al., 2015), and the primary visual cortex (V1; a primary sensory area for visual processing; Han et al., 2018; Hubel and Wiesel, 1959). The three cortical areas were virally injected individually or in combination. We first analyzed whole-brain imaging data with sparsely labeled neurons in the mPFC, ALM, or V1 by projecting raw fluorescence along the dorsal-ventral, anterior-posterior, and medial-lateral directions (Figures 4 and S3). Maximum-intensity projections of a typical mouse brain with a few dozens of mPFC neurons show surprisingly widespread projections across dozens of brain areas. The axonal arbors are extensive in several interbrain, midbrain, and hindbrain nuclei (Figure 4B), consistent with their diverse roles in behavioral control (Fuster, 2015; Miller, 2000; Otis et al., 2017). Despite the extensive projections, a vast majority of volume was screened out by our strategy for not imaging (Figure 4A). The whole-brain data with neurons in the ALM show similar characteristics (Figure 4C and 4D). However, neurons in the V1 seem to have many fewer long-range projections to subcortical areas (Figures S3A and S3B). SMART is not limited to brains with a single area labeled. We also imaged samples with sparsely labeled neurons in mPFC, ALM, and V1 in the same brain (Figures S3C and S3D).

By taking advantage of the sparsity of signals, we need to image only 11.1 ± 2.1% of the total brain volume (mean ± SD, Figures 5A and 5B). This results in a dramatic reduction in imaging time (25.6 ± 3.1 h for ALM, 27.3 ± 3.2 h for mPFC, and 14.2 ± 0.9 h for V1, mean ± SD, versus ∼204 h if all regions are imaged, Figures 5C and 5D), and produces a much reduced dataset size (2.7 ± 0.3 TB versus ∼31 TB if all regions are acquired at 16 bits). With labeled neurons in

Figure 2. Analysis of signal quality of SMART

(A) Histogram of SNR of axons in each tile from brain H241. Tiles were randomly selected (n = 386).

(B) Left: relationship between SNR of axonal terminals and their distance from cell bodies. Blue circles, data of individual tiles with axons. Orange circles, tiles shown on the right. Right: axons in tiles indicated by orange circles on the left (maximum-intensity projection). The background of each tile of the images can be slightly different, depending on the density of signals nearby that contribute to background through pinhole cross-talk in spinning-disk microscopy. Scale bar: 5 μm.

(C and D). Same format as in (A and B), respectively, but for 351 tiles from brain H236.

(E and F) Same format as in (A and B), respectively, but for 345 tiles from brain H244.

(G) Type of errors in signal detection. False positively (FP) detected cuboids are those imaged cuboids without fluorescent signal. Thus, FP cuboids add to the imaged volume that increases the total imaging time. False negatively (FN) detected surfaces are on the outer surfaces of the major titles that have fluorescent signals (*post hoc* checked by inspecting a few layers of images near the surface for axons and dendrites). FP surfaces lead to loss of signal and potential truncation of traced neurons.

(H) Fraction of FP and FN ratios. We optimized the FN ratio to be extremely low to avoid missing bright signals. Error bar: SD.

(I) Quantification of FN detected surfaces with signal. Of 0.13% FN detected surfaces, over 96% had low SNR. As low SNR renders tracing the full cell morphology extremely difficult, and we typically pick bright somata to trace, FN detected surfaces do not interfere with tracing the full axonal arbors.

(J) Quantification of SNR for signals on FN detected surfaces due to low SNR. Mean ± SD is 4.6 ± 2.1 (n = 47).

(K) Example of cases that lead to FN detected signals. In the top row, a segment of axon is present in the bottom surface of one section (left, section N) but the cuboid is not imaged using the 40× objective. The missing of signal is confirmed by the 16× and 40× objectives during imaging of the next section (section N + 1). In the bottom row, the signal is hardly visible in the 16× objective (left).

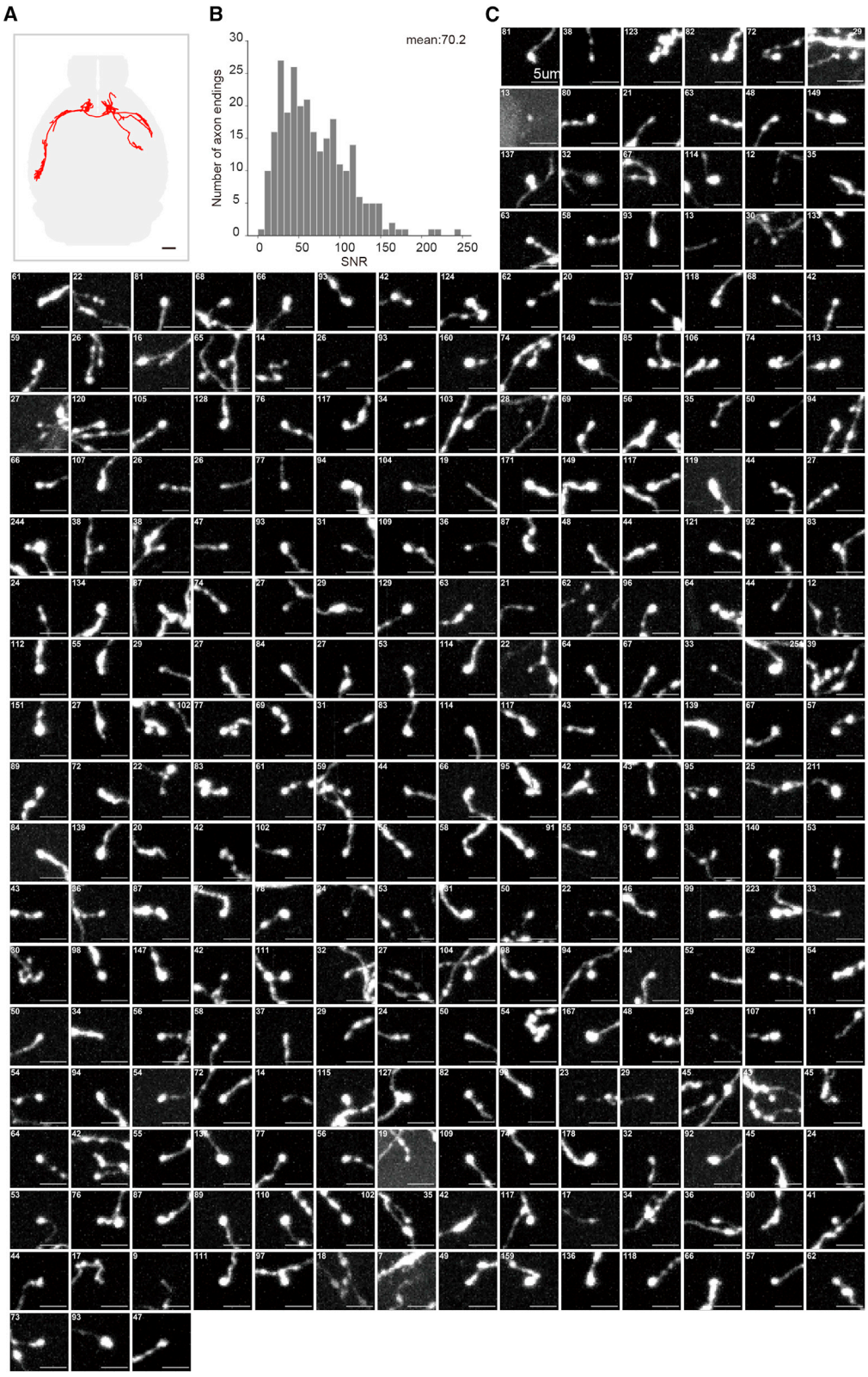

(legend on next page)

mPFC, ALM, and V1, the fraction of imaged volume is only roughly twice that with a single injected area (mPFC or ALM, Figure 5B). And the overall imaging time using the high-speed setup is similar to that with a single injected area (mPFC or ALM, Figure 5C). Notably, this increase in imaging speed is not at the cost of reduced resolution or SNR, and the high-resolution high-contrast method enables clear identification of individual axonal terminals (Figure 3).

Analysis of single neuronal morphology

We traced putative full morphology of 29 projection neurons in mPFC, ALM, or V1 (Figure 6A, see Figures S4 and S5 for full axonal morphology of each reconstructed neuron, and Figure S7 for local dendrites and axons). The processes of mPFC, ALM, and V1 neurons show differential distributions along the anteroposterior, mediolateral, and dorsoventral directions, reflecting their distinct projection targets (Figure 6B). The longest axonal path of mPFC neurons is significantly longer than those of ALM and V1 neurons, with ALM neurons also longer than V1 neurons (Figure 6C, t test, $p < 0.01$). The total axonal length shows a similar pattern (Figure 6D). The total axonal length is linearly correlated with the total number of branches (Figure 6E). Cortical projection neurons contain pyramidal tract (PT) and intratelencephalic (IT) neurons classified based on their distinct projection targets (Harris and Shepherd, 2015). Consistently, single-neuron reconstruction reveals that PT and IT neurons form different clusters (Figures 6F–6H), with distinct dendritic morphology and local axonal arbors (Figure S6), and project to different cortical and subcortical areas (Figures S7–S9). Most mPFC and V1 projection neurons have local axonal arbors (defined as axonal branches within 500 μm of a soma) while relatively few ALM neurons have local collaterals (70%–90% versus 25%, Figure S6). We further compared PT and IT neurons from mPFC and ALM (Figures 6I and S10). PT neurons from either mPFC or ALM tend to project more ipsilaterally, but with some contralateral projections in the thalamus, hypothalamus, and brain stem (Figures 6I, 7A, and 7B). PT neurons in mPFC bifurcate to target more brain areas compared with ALM neurons, with both mPFC and ALM neurons targeting much larger numbers of areas compared with V1 neurons (Figures 7C and 7D). Although ALM neurons on average have fewer targets, some of them have a massive number of terminals in one or two subcortical regions (for example, superior colliculus, motor related [SCm], Figure 6I). On average, PT neurons from mPFC have more projections in periaqueductal gray (PAG), while ALM have more in SCm, consistent with their roles in behavioral control (Lui et al., 2021) and orienting (Guo et al., 2014; Li et al., 2015), respectively. IT neurons from mPFC and ALM also tend to project more ipsilaterally (Figure S10).

DISCUSSION

We have developed a high-speed high-resolution high-contrast imaging system and demonstrated its capability in imaging and tracing individual neurons with fine axonal tracts and collaterals across the mouse brain. By taking advantage of sparse labeling, which is necessary for the reconstruction of fine axon collaterals using light microscopy, we have used the SMART system to image neurons in a variety of cortical regions within a few hours to a day, a much shorter time than previous methods (Table S1) (Economo et al., 2016; Gong et al., 2016; Li et al., 2010). This further demonstrates that real-time data analysis combined with instrument control can dramatically augment the performance of specific imaging systems (Long et al., 2017; Peng et al., 2014b; Zhang et al., 2021). There have been a number of alternative methods for whole-brain imaging, including knife-edge scanning microscopy, block-face two-photon or confocal microscopy, and light-sheet microscopy (Dodt et al., 2007; Economo et al., 2016; Gong et al., 2016; Li et al., 2010; Migliori et al., 2018; Narasimhan et al., 2017; Ragan et al., 2012; Seiriki et al., 2017; Wang et al., 2019a). The idea of sparse imaging may be adapted to these imaging approaches to increase the imaging speed without sacrificing resolution. Large-scale electron microscopy can image a small piece of tissue (typically much less than 1 mm^3) with nanometer resolution, and thus has the capability for dense reconstruction of neurites and synapses (Bock et al., 2011; Briggman et al., 2011; Morgan et al., 2016). With sparse imaging and tracing, mapping long-distance projections of single neurons using electron microscopy may be feasible in the future.

Visualizing the complete morphology of individual neurons is crucial to understand how the neurons implement their functions through dendritic and axonal processes. Neurons in the mPFC, ALM, and V1 show qualitatively different local and long-range axonal arbors, emphasizing their distinct roles in cognitive, movement, and sensory processing (Fuster, 2015; Guo et al., 2014; Han et al., 2018; Hubel and Wiesel, 1959; Li et al., 2015; Miller, 2000). Our system builds on a commercially available confocal scanning unit, and its fast speed, simple design, and lower requirement for data storage enable the system to be easily adapted in individual labs, facilitating routine use of whole-brain imaging for probing single-cell full morphology. The core of the SMART concept relies on efficient detection of regions with signals that typically requires volumetric imaging. We speed up this process by converting volumetric imaging into surface imaging of the volume as the neural process is essentially continuous. With SMART, we need to sample only roughly one-tenth the volume, and this consequently reduces the dataset by about 90%, greatly facilitating handling of large datasets. The pipeline is expected to greatly facilitate the investigation of single-neuron morphology through brain-wide imaging.

Figure 3. All axonal terminals of one mPFC neuron

(A) 3D visualization of the intratelencephalic neuron in the mPFC. Scale bar: 1 mm.

(B) Distribution of SNR for the axon endings (n = 265) in the example neuron. Signal was calculated using 3 × 3 pixels manually selected within each axonal ending. Noise was calculated using a rectangular background area without signal. SNR was the mean signal divided by the standard deviation of the background.

(C) Maximum-intensity projections (along the z axis) of all axonal terminals (n = 265) belonging to the mPFC neuron. The number on each small panel indicates the SNR for each axon terminal. All the images have the same intensity range. Scale bar: 5 μm.

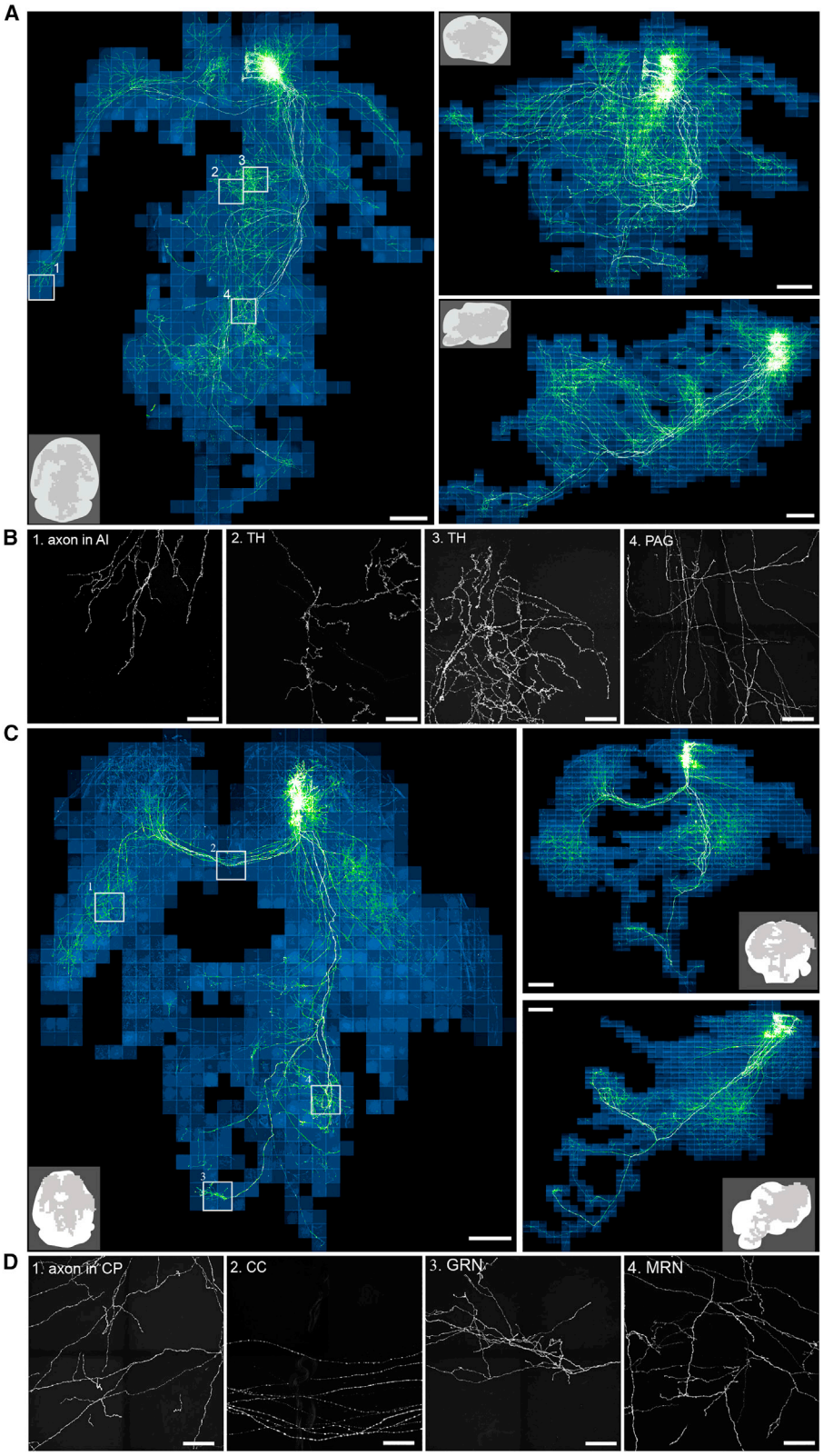

(legend on next page)

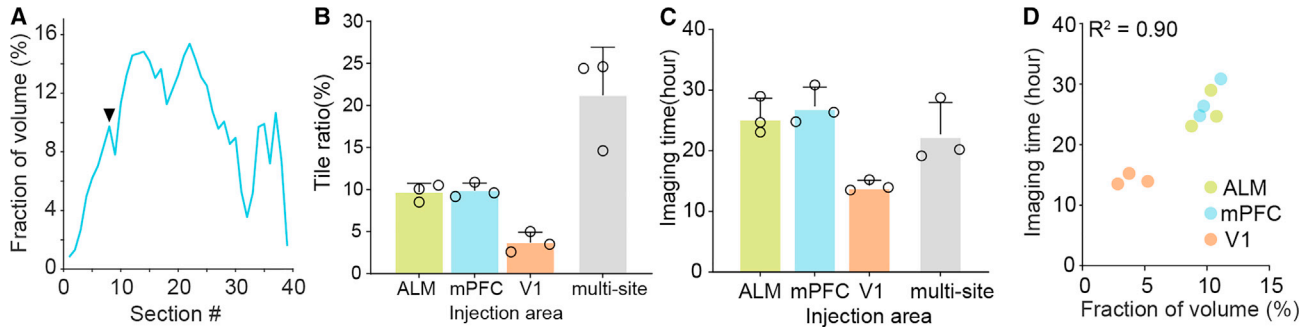

Figure 5. Acquisition time for whole-brain imaging of sparsely labeled neurons in various brain areas

(A) Fraction of imaged tiles in each section along the dorsal-ventral axis of a mouse brain. Solid downward-pointing triangle indicates the position of the example section in Figure 1C.

(B) Fraction of volume imaged with neurons labeled in various brain regions. Error bar: SD.

(C) Imaging time for brain samples in (B). Samples with labeled neurons in mPFC, ALM, and V1 (multi-sites injection) were imaged with the high-speed setup (STAR Methods). Error bar: SD.

(D) Imaging time is linearly correlated with the fraction of volume imaged.

See also Table S1.

Limitations of study

The concept of SMART relies on signal detection and imaging of signals with regional confinement. Neurons in individual regions typically project to one or two dozens of brain areas, leaving about 90% of brain tissue unlabeled. For brain-wide labeling through transgenic mouse lines, our approach will require a similar amount of time compared with cutting-edge high-resolution whole-brain imaging methods such as MOST (Gong et al., 2016; Li et al., 2010) and serial two-photon tomography (Economo et al., 2016). Under conditions that require brain-wide imaging, our setup can be used as a block-face spinning-disk system (Seiriki et al., 2017), diversifying its application for fast whole-brain imaging. Furthermore, we have demonstrated that SMART can still achieve ~10× speed-up with sparse labeling in three cortical areas when using the high-speed setup, lessening the requirement of sparse labeling.

STAR★METHODS

Detailed methods are provided in the online version of this paper and include the following:

- KEY RESOURCES TABLE
- RESOURCE AVAILABILITY
  - Lead contact
  - Materials availability
  - Data and code availability
- EXPERIMENTAL MODEL AND SUBJECT DETAILS
  - Mice
- METHOD DETAILS
  - Virus injection and sparse neuronal labeling
  - Tissue clearing and sample embedding for imaging
  - Whole brain imaging
  - Estimation of photobleaching
  - Signal detection
  - Image processing
- QUANTIFICATION AND STATISTICAL ANALYSIS
  - Annotation and visualization
  - Statistics

SUPPLEMENTAL INFORMATION

Supplemental information can be found online at https://doi.org/10.1016/j.crmeth.2021.100089.

ACKNOWLEDGMENTS

We thank Michael N. Economo for comments on the manuscript, Zhangcan Ding and Hanchuan Peng for help with Vaa3D software, Jiejue Li for tracing single neurons, Fan Di for help with viral injection and tissue clearing experiments, and the animal core facility at Tsinghua University for maintaining the mouse lines. This work was supported by grants from the National Natural Science Foundation of China (31871048, 32021002) and Tsinghua IDG/McGovern Institute for Brain Research (Brain + X) to Z.V.G.

Figure 4. Whole-brain imaging of sparsely labeled neurons in mPFC and ALM

(A) Maximum-intensity projections (MIPs) along the horizontal (left), coronal (right top), and sagittal (right bottom) directions of an SMART-imaged brain with about two dozen brightly labeled neurons in the mPFC. Scale bar: 1 mm.

(B) Zoom-in views of the numbered rectangular regions in (A) show axonal arbors in the agranular insular (AI), thalamus (TH), and midbrain periaqueductal gray (PAG). Axons in the TH show numerous varicosities. For clarity, 2 × 2 × 2 tiles along the x-y-z directions are shown for each region. Scale bar: 100 μm.

(C) The horizontal (left), coronal (right top), and sagittal (right bottom) MIPs of an SMART-imaged brain with a few dozens of brightly labeled neurons in the ALM. Scale bar: 1 mm.

(D) Zoom-in views of the numbered rectangular regions in (B) show axonal arbors in the caudoputamen (CP), corpus callosum (CC), gigantocellular reticular nucleus (GRN), and midbrain reticular nucleus (MRN). Axons in the CC are clearly beaded. Same format as in (B). Scale bar: 100 μm.

See also Figures S2 and S3.

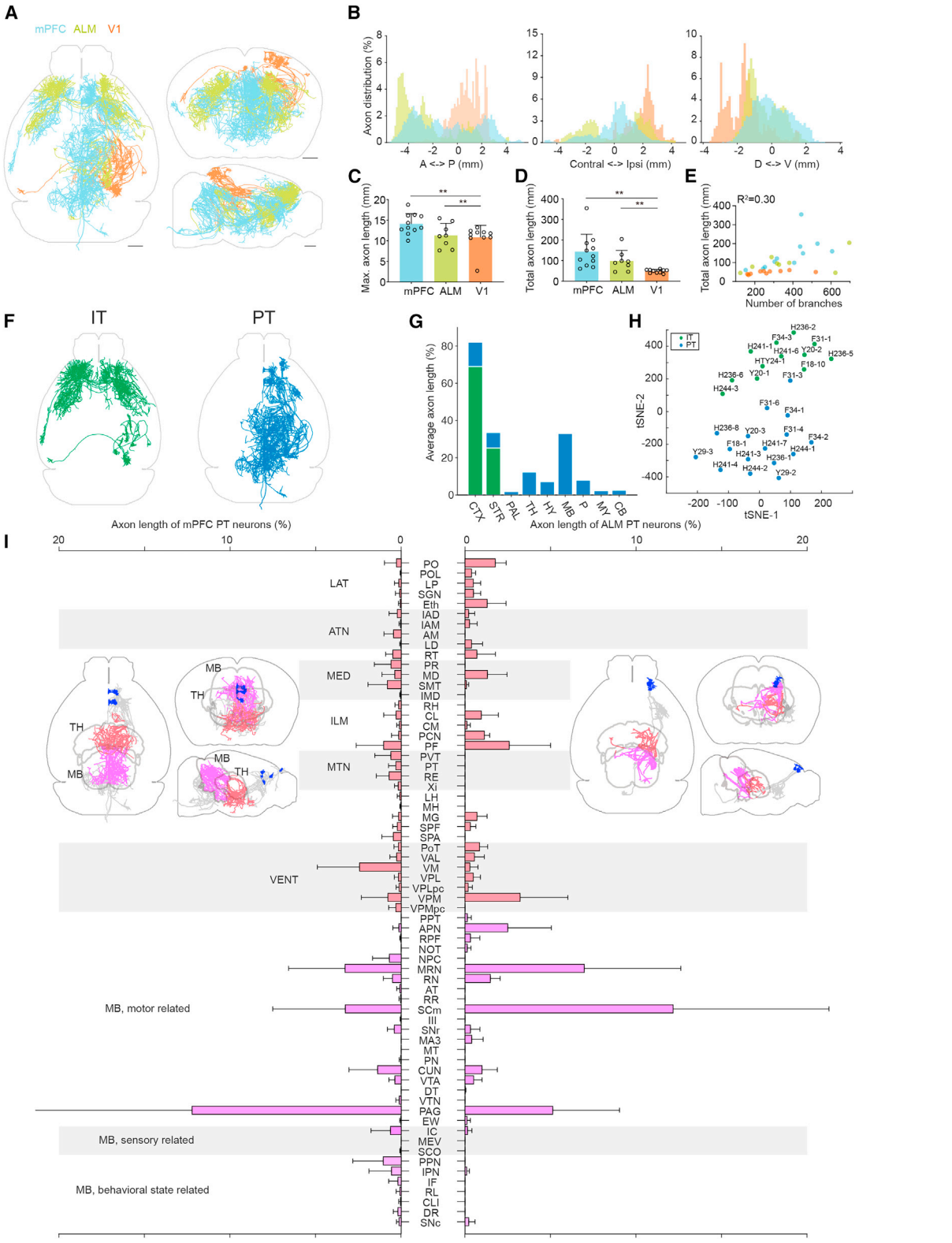

Figure 6. Analyses of morphological features of mPFC, ALM, and V1 neurons

(A) Brain-wide projection of neuronal processes of traced individual neurons along the horizontal (left), coronal (right top), and sagittal (right bottom) directions. Blue, mPFC neurons; green, ALM neurons; orange, V1 neurons. Scale bar: 1 mm.

(legend continued on next page)

CellPress
OPEN ACCESS

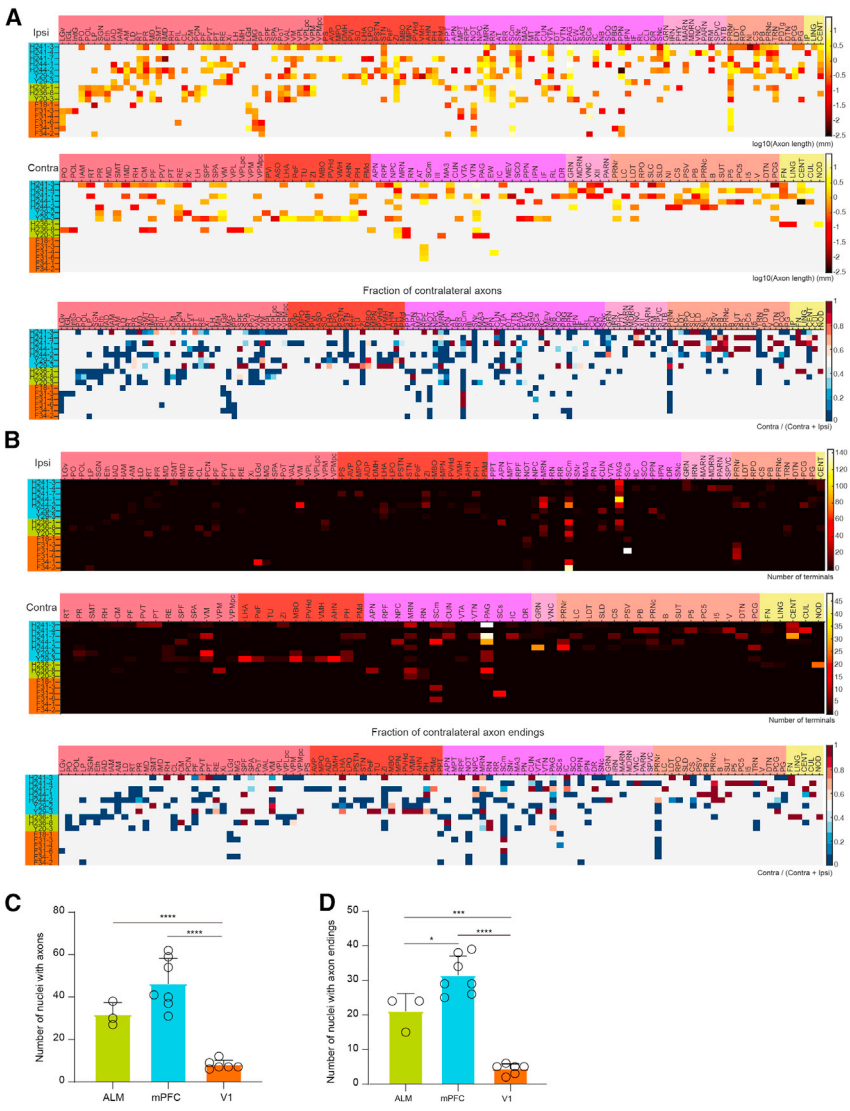

Figure 7. Long-range projections of pyramidal tract neurons in mPFC, ALM, and V1

(A) Total axon length of individual neurons in different cortical and subcortical areas in the ipsilateral (top) or contralateral (middle) hemisphere. The normalized fraction of axon length in the contralateral hemisphere (to total axon length) is shown in the bottom row. There are typically fewer contralateral projections. Blue, mPFC neurons; green, ALM neurons; orange, V1 neurons.

(B) Number of axonal terminals in the ipsilateral (top) or contralateral (middle) hemisphere. Note the difference in color bar for the top and middle rows. There are typically fewer terminals in the contralateral hemisphere.

(C) Number of nuclei with axons for mPFC, ALM, and V1 neurons. mPFC and ALM neurons project more extensively than V1 neurons. Error bar: SD. *$p < 0.05$, ****$p < 0.0001$ (unpaired t test).

(D) Number of nuclei with axonal terminals for mPFC, ALM, and V1 neurons. Error bar: SD. *$p < 0.05$, ***$p < 0.001$, ****$p < 0.0001$ (unpaired t test).

See also Figure S10.

AUTHOR CONTRIBUTIONS

H.C. built the imaging setup, wrote the image acquisition code, acquired whole-brain imaging data, and performed data analysis. T.H. performed sparse labeling, cleared mouse brains, built the image processing pipeline, and analyzed single-neuron data. Y.Y. acquired whole-brain imaging data and performed data analysis. T.H., Y.Y., X.Y., Y.H., Y.W., W.Z., R.J., and H.Y. traced single neurons. Z.V.G. conceived and supervised the project. H.C., T.H., Y.Y., and Z.V.G. wrote the paper with comments from other authors.

(B) Distribution of axons along the anterior-posterior (AP), contralateral-ipsilateral, and dorsal-ventral (DV) directions. Bregma is chosen as the origin along the AP and contralateral-ipsilateral directions, while the centroid of the brain is chosen as the origin along the DV direction.

(C) The maximum axon length of mPFC (n = 11), ALM (n = 8), and V1 (n = 10) neurons. Error bar: SD. **$p < 0.01$ (unpaired t test).

(D) The total axon length of mPFC, ALM, and V1 neurons. V1 neurons on average have much shorter total axon length compared with mPFC and ALM neurons. Same number of neurons as in (C). Errr bar: SD. **$p < 0.01$ (unpaired t test).

(E) The total axon length is close to linearly correlated with the number of branches.

(F) Brain-wide projection of IT and PT neurons.

(G) Distribution of axons in different brain areas for IT and PT neurons. The axon length in each area is normalized to the total axon length. The sum of the normalized axon length does not reach 1, as there are *en passant* axons in white matter.

(H) t-SNE shows clustering of IT and PT neurons.

(I) Distribution of long-range axons of mPFC and ALM PT neurons in the thalamus (TH) and midbrain (MB) nuclei. LAT, ATN, MED, ILM, MTN, VENT are different groups of thalamic nuclei. Error bar: SD.

See also Figures S4–S10.

DECLARATION OF INTERESTS

The authors declare no competing interest.

Received: May 26, 2021
Revised: August 12, 2021
Accepted: September 3, 2021
Published: October 1, 2021

REFERENCES

Alexander, G.E., Crutcher, M.D., and DeLong, M.R. (1990). Basal ganglia-thalamocortical circuits: parallel substrates for motor, oculomotor, "prefrontal" and "limbic" functions. Prog. Brain Res. *85*, 119–146.

Bock, D.D., Lee, W.C., Kerlin, A.M., Andermann, M.L., Hood, G., Wetzel, A.W., Yurgenson, S., Soucy, E.R., Kim, H.S., and Reid, R.C. (2011). Network anatomy and in vivo physiology of visual cortical neurons. Nature *471*, 177–182.

Briggman, K.L., Helmstaedter, M., and Denk, W. (2011). Wiring specificity in the direction-selectivity circuit of the retina. Nature *471*, 183–188.

Dodt, H.U., Leischner, U., Schierloh, A., Jahrling, N., Mauch, C.P., Deininger, K., Deussing, J.M., Eder, M., Zieglgansberger, W., and Becker, K. (2007). Ultramicroscopy: three-dimensional visualization of neuronal networks in the whole mouse brain. Nat. Methods *4*, 331–336.

Economo, M.N., Clack, N.G., Lavis, L.D., Gerfen, C.R., Svoboda, K., Myers, E.W., and Chandrashekar, J. (2016). A platform for brain-wide imaging and reconstruction of individual neurons. eLife *5*, e10566.

Felleman, D.J., and Van Essen, D.C. (1991). Distributed hierarchical processing in the primate cerebral cortex. Cereb. Cortex *1*, 1–47.

Feng, G., Mellor, R.H., Bernstein, M., Keller-Peck, C., Nguyen, Q.T., Wallace, M., Nerbonne, J.M., Lichtman, J.W., and Sanes, J.R. (2000). Imaging neuronal subsets in transgenic mice expressing multiple spectral variants of GFP. Neuron *28*, 41–51.

Fuster, J.M. (2015). The Prefrontal Cortex, Fifth Edition (Elsvier Ltd.).

Gerfen, C.R., and Sawchenko, P.E. (1984). An anterograde neuroanatomical tracing method that shows the detailed morphology of neurons, their axons and terminals: immunohistochemical localization of an axonally transported plant lectin, Phaseolus vulgaris leucoagglutinin (PHA-L). Brain Res. *290*, 219–238.

Ghosh, S., Larson, S.D., Hefzi, H., Marnoy, Z., Cutforth, T., Dokka, K., and Baldwin, K.K. (2011). Sensory maps in the olfactory cortex defined by long-range viral tracing of single neurons. Nature *472*, 217–220.

Glasser, M.F., Coalson, T.S., Robinson, E.C., Hacker, C.D., Harwell, J., Yacoub, E., Ugurbil, K., Andersson, J., Beckmann, C.F., Jenkinson, M., et al. (2016). A multi-modal parcellation of human cerebral cortex. Nature *536*, 171–178.

Glickfeld, L.L., Andermann, M.L., Bonin, V., and Reid, R.C. (2013). Cortico-cortical projections in mouse visual cortex are functionally target specific. Nat. Neurosci. *16*, 219–226.

Gong, H., Xu, D., Yuan, J., Li, X., Guo, C., Peng, J., Li, Y., Schwarz, L.A., Li, A., Hu, B., et al. (2016). High-throughput dual-colour precision imaging for brain-wide connectome with cytoarchitectonic landmarks at the cellular level. Nat. Commun. *7*, 12142.

Guo, Z.V., Inagaki, H.K., Daie, K., Druckmann, S., Gerfen, C.R., and Svoboda, K. (2017). Maintenance of persistent activity in a frontal thalamocortical loop. Nature *545*, 181–186.

Guo, Z.V., Li, N., Huber, D., Ophir, E., Gutnisky, D., Ting, J.T., Feng, G., and Svoboda, K. (2014). Flow of cortical activity underlying a tactile decision in mice. Neuron *81*, 179–194.

Han, Y., Kebschull, J.M., Campbell, R.A.A., Cowan, D., Imhof, F., Zador, A.M., and Mrsic-Flogel, T.D. (2018). The logic of single-cell projections from visual cortex. Nature *556*, 51–56.

Harris, K.D., and Shepherd, G.M. (2015). The neocortical circuit: themes and variations. Nat. Neurosci. *18*, 170–181.

Heeger, D.J., and Ress, D. (2002). What does fMRI tell us about neuronal activity? Nat. Rev. Neurosci. *3*, 142–151.

Hubel, D.H., and Wiesel, T.N. (1959). Receptive fields of single neurones in the cat's striate cortex. J. Physiol. *148*, 574–591.

Klein, S., Staring, M., Murphy, K., Viergever, M.A., and Pluim, J.P. (2010). elastix: a toolbox for intensity-based medical image registration. IEEE Trans. Med. Imaging *29*, 196–205.

Kuan, L., Li, Y., Lau, C., Feng, D., Bernard, A., Sunkin, S.M., Zeng, H., Dang, C., Hawrylycz, M., and Ng, L. (2015). Neuroinformatics of the allen mouse brain connectivity atlas. Methods *73*, 4–17.

Kuramoto, E., Furuta, T., Nakamura, K.C., Unzai, T., Hioki, H., and Kaneko, T. (2009). Two types of thalamocortical projections from the motor thalamic nuclei of the rat: a single neuron-tracing study using viral vectors. Cereb. Cortex *19*, 2065–2077.

Lai, H.M., Liu, A.K.L., Ng, H.H.M., Goldfinger, M.H., Chau, T.W., DeFelice, J., Tilley, B.S., Wong, W.M., Wu, W., and Gentleman, S.M. (2018). Next generation histology methods for three-dimensional imaging of fresh and archival human brain tissues. Nat. Commun. *9*, 1066.

Li, A., Gong, H., Zhang, B., Wang, Q., Yan, C., Wu, J., Liu, Q., Zeng, S., and Luo, Q. (2010). Micro-optical sectioning tomography to obtain a high-resolution atlas of the mouse brain. Science *330*, 1404–1408.

Li, N., Chen, T.W., Guo, Z.V., Gerfen, C.R., and Svoboda, K. (2015). A motor cortex circuit for motor planning and movement. Nature *519*, 51–56.

Lin, R., Wang, R., Yuan, J., Feng, Q., Zhou, Y., Zeng, S., Ren, M., Jiang, S., Ni, H., Zhou, C., et al. (2018). Cell-type-specific and projection-specific brain-wide reconstruction of single neurons. Nat. Methods *15*, 1033–1036.

Long, B., Zhou, Z., Cetin, A., Ting, J., Gwinn, R., Tasic, B., Daigle, T., Lein, E., Zeng, H., Saggau, P., et al. (2017). SmartScope2: Simultaneous imaging and reconstruction of neuronal morphology. Sci. Rep. *7*, 9325.

Lui, J.H., Nguyen, N.D., Grutzner, S.M., Darmanis, S., Peixoto, D., Wagner, M.J., Allen, W.E., Kebschull, J.M., Richman, E.B., Ren, J., et al. (2021). Differential encoding in prefrontal cortex projection neuron classes across cognitive tasks. Cell *184*, 489–506 e426.

Luppi, P.H., Fort, P., and Jouvet, M. (1990). Iontophoretic application of unconjugated cholera toxin B subunit (CTb) combined with immunohistochemistry of neurochemical substances: a method for transmitter identification of retrogradely labeled neurons. Brain Res. *534*, 209–224.

Mainen, Z.F., and Sejnowski, T.J. (1996). Influence of dendritic structure on firing pattern in model neocortical neurons. Nature *382*, 363–366.

Migliori, B., Datta, M.S., Dupre, C., Apak, M.C., Asano, S., Gao, R., Boyden, E.S., Hermanson, O., Yuste, R., and Tomer, R. (2018). Light sheet theta microscopy for rapid high-resolution imaging of large biological samples. BMC Biol. *16*, 57.

Miller, E.K. (2000). The prefrontal cortex and cognitive control. Nat. Rev. Neurosci. *1*, 59–65.

Morgan, J.L., Berger, D.R., Wetzel, A.W., and Lichtman, J.W. (2016). The fuzzy logic of network connectivity in mouse visual thalamus. Cell *165*, 192–206.

Murakami, T.C., Mano, T., Saikawa, S., Horiguchi, S.A., Shigeta, D., Baba, K., Sekiya, H., Shimizu, Y., Tanaka, K.F., Kiyonari, H., et al. (2018). A three-dimensional single-cell-resolution whole-brain atlas using CUBIC-X expansion microscopy and tissue clearing. Nat. Neurosci. *21*, 625–637.

Narasimhan, A., Umadevi Venkataraju, K., Mizrachi, J., Albeanu, D.F., and Osten, P. (2017). Oblique light sheet tomography: fast and high resolution volumetric imaging of mouse brains. bioRxiv. https://doi.org/10.1101/132423.

Oh, S.W., Harris, J.A., Ng, L., Winslow, B., Cain, N., Mihalas, S., Wang, Q., Lau, C., Kuan, L., Henry, A.M., et al. (2014). A mesoscale connectome of the mouse brain. Nature *508*, 207–214.

Otis, J.M., Namboodiri, V.M., Matan, A.M., Voets, E.S., Mohorn, E.P., Kosyk, O., McHenry, J.A., Robinson, J.E., Resendez, S.L., Rossi, M.A., et al. (2017). Prefrontal cortex output circuits guide reward seeking through divergent cue encoding. Nature *543*, 103–107.

Peng, H., Bria, A., Zhou, Z., Iannello, G., and Long, F. (2014a). Extensible visualization and analysis for multidimensional images using Vaa3D. Nat. Protoc. *9*, 193–208.

Peng, H., Ruan, Z., Long, F., Simpson, J.H., and Myers, E.W. (2010). V3D enables real-time 3D visualization and quantitative analysis of large-scale biological image data sets. Nat. Biotechnol. *28*, 348–353.

Peng, H., Tang, J., Xiao, H., Bria, A., Zhou, J., Butler, V., Zhou, Z., Gonzalez-Bellido, P.T., Oh, S.W., Chen, J., et al. (2014b). Virtual finger boosts three-dimensional imaging and microsurgery as well as terabyte volume image visualization and analysis. Nat. Commun. *5*, 4342.

Ragan, T., Kadiri, L.R., Venkataraju, K.U., Bahlmann, K., Sutin, J., Taranda, J., Arganda-Carreras, I., Kim, Y., Seung, H.S., and Osten, P. (2012). Serial two-photon tomography for automated ex vivo mouse brain imaging. Nat. Methods *9*, 255–258.

Sanes, J.R., and Masland, R.H. (2015). The types of retinal ganglion cells: current status and implications for neuronal classification. Annu. Rev. Neurosci. *38*, 221–246.

Seiriki, K., Kasai, A., Hashimoto, T., Schulze, W., Niu, M., Yamaguchi, S., Nakazawa, T., Inoue, K.-i., Uezono, S., Takada, M., et al. (2017). High-speed and scalable whole-brain imaging in rodents and primates. Neuron *94*, 1085–1100.e1086.

Susaki, E.A., Tainaka, K., Perrin, D., Kishino, F., Tawara, T., Watanabe, T.M., Yokoyama, C., Onoe, H., Eguchi, M., Yamaguchi, S., et al. (2014). Whole-brain imaging with single-cell resolution using chemical cocktails and computational analysis. Cell *157*, 726–739.

Tustison, N.J., Cook, P.A., Klein, A., Song, G., Das, S.R., Duda, J.T., Kandel, B.M., van Strien, N., Stone, J.R., Gee, J.C., et al. (2014). Large-scale evaluation of ANTs and FreeSurfer cortical thickness measurements. NeuroImage *99*, 166–179.

Veenman, C.L., Reiner, A., and Honig, M.G. (1992). Biotinylated dextran amine as an anterograde tracer for single- and double-labeling studies. J. Neurosci. Methods *41*, 239–254.

Wang, Y., Yin, X., Zhang, Z., Li, J., Zhao, W., and Guo, Z.V. (2021). A cortico-basal ganglia-thalamo-cortical channel underlying short-term memory. Neuron. https://doi.org/10.1016/j.neuron.2021.08.002.

Wang, H., Zhu, Q., Ding, L., Shen, Y., Yang, C.-Y., Xu, F., Shu, C., Guo, Y., Xiong, Z., Shan, Q., et al. (2019a). Scalable volumetric imaging for ultrahigh-speed brain mapping at synaptic resolution. Natl. Sci. Rev. *6*, 982–992.

Wang, Q., Ding, S.L., Li, Y., Royall, J., Feng, D., Lesnar, P., Graddis, N., Naeemi, M., Facer, B., Ho, A., et al. (2020). The allen mouse brain Common coordinate Framework: a 3D reference atlas. Cell *181*, 936–953 e920.

Wang, Y., Xie, P., Gong, H., Zhou, Z., Kuang, X., Wang, Y., Li, A.-a., Li, Y., Liu, L., Veldman, M.B., et al. (2019b). Complete single neuron reconstruction reveals morphological diversity in molecularly defined claustral and cortical neuron types. bioRxiv. https://doi.org/10.1101/675280.

Winnubst, J., Bas, E., Ferreira, T.A., Wu, Z., Economo, M.N., Edson, P., Arthur, B.J., Bruns, C., Rokicki, K., Schauder, D., et al. (2019). Reconstruction of 1,000 projection neurons reveals new cell types and organization of long-range connectivity in the mouse brain. Cell *179*, 268–281 e213.

Wu, H., Williams, J., and Nathans, J. (2014). Complete morphologies of basal forebrain cholinergic neurons in the mouse. eLife *3*, e02444.

Xu, N.L., Harnett, M.T., Williams, S.R., Huber, D., O'Connor, D.H., Svoboda, K., and Magee, J.C. (2012). Nonlinear dendritic integration of sensory and motor input during an active sensing task. Nature *492*, 247–251.

Zhang, Z., Yao, X., Yin, X., Ding, Z., Huang, T., Huo, Y., Ji, R., Peng, H., and Guo, Z.V. (2021). Multi-scale light-sheet fluorescence microscopy for fast whole brain imaging. Front. Neuroanat. *15*, 732464.

Zingg, B., Hintiryan, H., Gou, L., Song, M.Y., Bay, M., Bienkowski, M.S., Foster, N.N., Yamashita, S., Bowman, I., Toga, A.W., et al. (2014). Neural networks of the mouse neocortex. Cell *156*, 1096–1111.

STAR★METHODS

KEY RESOURCES TABLE

REAGENT or RESOURCE	SOURCE	IDENTIFIER
Bacterial and virus strains		
pENN-AAV-hSyn-Cre-WPRE-hGH	James M. Wilson	Addgene 105553-AAV1;
AAV-pCAG-FLEX-EGFP-WPRE	Hongkui Zeng	Addgene 51502-AAV1
Chemicals, peptides, and recombinant proteins		
Urea	Sigma-Aldrich	51456, CAS:57-13-6
Triton X-100	Sigma-Aldrich	T9284, CAS:9002-93-1
N,N,N′,N′-Tetramethylethylenediamine	Sigma-Aldrich	NB20130, CAS:110-18-9
Histodenz	Sigma-Aldrich	D2158, CAS: 66108-95-0
N-Methyl-D-glucamine	Sigma-Aldrich	M2004, CAS: 6248-40-8
PBS(10X)	ThermoFisher	70011069
Experimental models: organisms/strains		
Mouse: C57BL/6J	Vital River	219
Software and algorithms		
MATLAB 2017b & 2018b	MathWorks	https://www.mathworks.com/products/MATLAB.html; RRID: SCR_001622
LabVIEW	National Instruments	http://www.ni.com/enus/shop/labview.htm; RRID: SCR_014325
Elastix	Klein et al. (2010)	RRID:SCR_009619
ANTs	Tustison et al. (2014)	RRID:SCR_004757
Vaa3d	Peng et al. (2010)	RRID:SCR_002609
Other		
488nm laser	Obis LX/LS	OBIS 488-150 mW
Confocal scanner unit	Yokogawa Electronic	CSU-W1
180 mm tube lens	Olympus	U-TLU
Motorized X-Y-Z stages	Thorlabs	LNR50SE/M
40x oil immersion objective	Olympus	UPlanFLN
16x water immersion objective	Nikon	N16XLWD-PF
25x multi-immersion objective	Olympus	XLSLPLN25XGMP
10x multi-immersion objective	Olympus	XLPLN10XSVMP
Piezo objective positioner	Thorlabs	PFM450E
Motorized stage	Zaber	X-LSQ075B
Motorized stage	Henggong	HGTA0850
sCMOS camera	Teledyne Photometrics	Prime 95B
I/O Device	National Instruments	USB-6366
Vibratome	Leica	VT1200
Source code	This paper	https://doi.org/10.5281/zenodo.5346760

RESOURCE AVAILABILITY

Lead contact

Further information and requests for resources and reagents should be directed to and will be fulfilled by the lead contact, Zengcai V. Guo (guozengcai@tsinghua.edu.cn).

Materials availability

This study did not generate new unique reagents.

Data and code availability

- The data of single neuron morphology generated during this study are available at https://github.com/NeuralCircuits-Behavior/Chen-Huang-Yang-et-al-2021 (https://doi.org/10.5281/zenodo.5346760).
- The code for hardware control and imaging generated during this study will be available at https://github.com/NeuralCircuits-Behavior/Chen-Huang-Yang-et-al-2021 (https://doi.org/10.5281/zenodo.5346760).
- Any additional information required to reanalyze the data reported in this work is available from the lead contact upon reasonable request.

EXPERIMENTAL MODEL AND SUBJECT DETAILS

Mice

C57BL/6J adult male mice (8–15 weeks) were used for sparse labeling and imaging experiments. Mice were maintained on a 12/12-hour light/dark cycle, and at 22–26°C with sterile pellet food and water *ad libitum*. All animal experiments used in this study were approved by the IACUC (Institutional Animal Care and Use Committee) of Tsinghua University.

METHOD DETAILS

Virus injection and sparse neuronal labeling

To achieve sparse labeling of a few dozens of cortical neurons, a mixture of AAV2/1-hSyn-Cre (final titer $\sim 5 \times 10^7$ GC/mL) and AAV2/1-CAG-Flex-EGFP ($\sim 2 \times 10^{12}$ GC/mL) was injected (Economo et al., 2016). The injection procedure was similar as before (Wang et al., 2021). Mice were kept anesthetized under 1–2% isoflurane during the whole injection procedure. The viral mixture was delivered through an oil hydraulic micromanipulator (Narishige, MO-10, ~17 nL/min for 50 nL) into mPFC (injection site, AP: +1.85, ML: 0.4, DV: 1.7), ALM (AP: +2.5, ML: 1.5, DV: 0.7), and V1 (AP: −3.78, ML: 2.3, DV: 0.6). Each mouse was injected unilaterally in one selected cortical area (mPFC, ALM or V1) or in three cortical areas (mPFC, ALM and V1). Mice were maintained for 5 weeks to allow stable and strong expression of EGFP.

Tissue clearing and sample embedding for imaging

Five weeks after virus injection, mice were anesthetized with 0.5% pentobarbital sodium solution (0.4 mL/30 g body weight), and transcardially perfused with 0.1 M PBS containing 20 U/ml heparin. The internal liquid pressure during perfusion was adjusted to be low (~70 mmHg) during the first 10 min of perfusion, followed by another 10 min at a higher pressure (~100 mmHg). We found the higher pressure potentially reduced autofluorescence from blood vessels that interfered detection of neuronal signal during imaging. After PBS, mice were perfused with 4% paraformaldehyde (PFA) in 0.1M PB.

Brains were dissected and post-fixed in 4% PFA for about 2 days at 4°C. After washing in PBS for 1 day (solution changed at 6 h and 12 h), brain samples were delipidated with CUBIC-1 solution for 6 days at room temperature (solution changed at day 3 and day 5) (Murakami et al., 2018). Alternatively, if brain samples were not needed urgently, samples were delipidated for 16 days at 4°C (solution changed at day 4, 8 and 12). Following washing in PBS for 1.5 days with solution changed at 6 h, 12 h, and 24 h, brain samples were immersed in refractive index matching solution OPTIClear for another 1.5 days at room temperature with solution changed at 6 h, 12 h and 24 h (Lai et al., 2018).

After refractive index matching, brain samples were embedded in 3–4% agarose dissolved in OPTIClear solution (Lai et al., 2018). The agarose gel cannot be glued well to the substrate for imaging. Thus, the embedded brain samples were further embedded in 4% agarose dissolved in OPTIClear solution (but without the N-methylglucamine component for better adherence), and then glued on the sample stage using instant adhesive (Loctite 401). Alternatively, the embedded brain samples were mechanically clamped on the sample stage to avoid the gluing process.

To measure the degradation of signal along the imaging depth, we imaged a cleared thy1-YFP-H transgenic mouse brain (Feng et al., 2000). Brightness of somata at each depth was quantified in ImageJ.

Whole brain imaging

For excitation, light from a 488nm laser (Obis LX/LS, Coherent) passed a Nipkow disk-based confocal scanner unit (CSU-W1; Yokogawa Electronic), a tube lens (U-TLU, Olympus), and an objective to reach brain samples that were fixed on motorized X-Y-Z stages with optical encoders (LNR50SE/M, Thorlabs). We adopted two sets of objectives: a high-resolution high-sensitivity set for weak fluorescence imaging and a high-speed set for faster whole brain imaging. The former consisted of a 40x oil immersion objective (UPlanFLN, NA1.3, Olympus) and a 16x water immersion objective (N16XLWD-PF, NA 0.80, Nikon). The 40x oil objective was attached to a piezo objective positioner (PFM450E, Thorlabs) for fast Z scanning. The 16x objective provided a larger field of view

and was used to quickly scan the sample to detect fluorescent signals. A customized dipping cap was attached to the 16x objective to reduce spherical aberration due to mismatch of refractive index of immersion solution. As we used an Olympus tube lens with a focal length of 180mm, the 16x Nikon objective had an effective magnification of 14.4×. The 40x and 16x objectives were assembled in a dual-objective nosepiece that was attached to a motorized stage (X-LSQ075B, Zaber) to enable fast switching of objectives. In addition, the Zaber stage was attached to a motorized stage (HGTA0850, Henggong) in order to correct the mismatch of focal planes of the two objectives. The emitted fluorescence passed the objective, tube lens, confocal scanner unit equipped with a band-pass filter (525 ± 25 nm) to reach a back-illuminated sCMOS camera (Prime 95B, Teledyne Photometrics) that was triggered by a multi-functional I/O Device (USB-6366, National Instruments). After imaging the top section of brain sample (250 μm), a thin section (195 μm) was cut off by a vibratome (VT1200, Leica) to leave ~55 μm of overlap between sections. In the high-speed configuration, we used a 25x and a 10x multi-immersion objective (XLSLPLN25XGMP, NA 1.0; XLPLN10XSVMP, NA 0.6, Olympus), corresponding to the 40x and 16x objectives in the high-resolution configuration. All results were obtained with the high-resolution configuration if not specified.

Whole-brain imaging was performed by repeating the following steps (for the high-resolution set of objectives). First, XY stages automatically moved along the tissue edge and acquired images to determine the boundary of imaging area using the 16x objective. Second, the whole imaging area was divided into overlapping tiles according to the image size using the 16x objective. For each tile, a set of 9 images with 30 μm spacing along the z axis were acquired. As the camera chip has a size of 13.2 × 13.2 mm^2, each tile covered about 917 × 917 μm^2 area with 22.5 μm overlap in XY directions between adjacent tiles. The maximum intensity projected image (along the z axis) was analyzed by a custom written script in MATLAB (MathWorks) to detect fluorescent signals (see signal detection). The Z-projected image was then divided into 3 x 3 subregions. Third, subregions with neuronal signals were pushed into a queue for imaging using the 40x objective. The stack acquired with the 40x objective covered 330× 330 μm^2 with ~30 μm overlap in XY directions. As the 40x objective had a short working distance of ~400 μm, we chose each stack to span ~250 μm in the axial direction. The piezo objective positioner moved at 1 μm step and thus the voxel size using the 40x objective was ~0.3 × 0.3 × 1.0 μm^3. After each successful movement, a voltage signal triggered camera to acquire a high-resolution image. For each acquired stack, the sides (~5% of width along each direction) was maximum intensity projected and the projected images were analyzed using a custom written script to determine whether there were fluorescent signals (see signal detection). If there were signals detected on one side, then the neighboring tile was pushed into the imaging queue. Imaging of each tile was repeated until the queue was empty. Finally, the imaged section was trimmed off using a vibratome. The overlap between sections was 55 μm.

For the high-speed configuration, a set of 17 images with 15–30 μm spacing along the z axis was acquired with the 10x objective. Each tile covered about 1320 × 1320 μm^2 area with 132 μm overlap in XY directions between adjacent tiles. The stack acquired with 25x objective was 528× 528 × 400 μm^3 with ~70 μm overlap in XY directions (voxel size ~0.4 × 0.4 × 1.0 μm^3). We chose each stack to span 400 μm to roughly match the size of the stack in XY directions. The overlap between sections was 55 μm. The 25x objective has a long working distance (8 mm) that enables deeper imaging. Thus each section was imaged starting 400 μm below the cutting plane to reduce tissue distortion as deformation induced by mechanical cutting decayed along depth.

Estimation of photobleaching

Our cleared brain samples are nearly transparent which potentially causes photobleaching of fluorescent proteins within the cone of light propagation. The mouse brains were imaged along the dorsal-ventral direction that spans ~6 mm. If we assume excitation light does not expand during propagation (equivalent to the case of using objectives with NA<<1), fluorescent proteins near the ventral surface will be illuminated during exposure for each image above. As we used a 1 μm imaging step along the Z direction, this equivalents to 6000 exposures, or 2 minutes as each image requires 20 ms light exposure. In another extreme condition, if we assume excitation light expands to cover every slice below (equivalent to the case with NA close to the refractive index of mounting media), the light intensity on each slice will be 1/N of the original intensity I (assuming light just propagates to fill in each brain slice and no more, yielding an upper bound of estimation of light intensity). As there are on average N images on each slice and there are 6000 slices, fluorescent proteins near the ventral surface will be illuminated with total intensity of N x I/N x 6000 (equivalent to 2 minutes of total exposure at the in-focus intensity). We also simulated the effect of photobleaching based on the size of field of view of the spinning disk, light propagation angle of the 40x oil objective (NA 1.3), and our imaged stacks using the SMART system (with consideration of extra imaging in overlapped regions). We found that on average each location was illuminated from 1 min in V1 to 1.8 min in mPFC samples (Figure S2D). With the calibrated photobleaching rate, we estimated that this reduced fluorescent signal by 11–19%. Consistently, we did not observe obvious intensity drop in axons with increased distance from somata (Figure 2).

Signal detection

A custom written program in MATLAB (MathWorks) was used to semi-automatically detect fluorescent signals. Edge and line detection methods was first applied to automatically detect signals from the maximum intensity projected image acquired using the 16x objective (Kuan et al., 2015). Then manual inspection was used to improve the detection accuracy. For finer images acquired using 40x objective, intensity above a conservative threshold (~140 units above background, i.e. high threshold) was used to classify images with signals. As intensity in the background region was ~2–5 units above background, images with 140 units above background almost always had signals. Images with intensity below a threshold (~10–25 units above background, depending on the level of noise) was automatically classified as without signals. In practice, faint signals with SNR below ~3–5 were hard to trace. Images

with maximum intensity in between were manually inspected for signals or alternatively were imaged automatically without further inspection (this approach reached a similar accuracy in detecting signals but produced more empty regions to image, and thus increased imaging time).

We analyzed false positive (FP) and false negative (FN) rate of signal detection by examining image stacks acquired using 40x objective. There were two types of FP tiles, with Type I referring to isolated tiles that did not connect to labeled neurons and Type II tiles that did not have any fluorescent signals inside despite that these tiles were connected to tiles with fluorescent signals (Figure 2G). Type I tiles were not connected to the cluster of tiles with fluorescent signals and were counted directly after imaging. Type II tiles were identified by manually checking the maximum intensity projection of all tiles after imaging. The FP rate is defined by the ratio of the number of Type I and Type II tiles to the total imaged tiles. Thus, the FP rate reflected the percentage of tiles imaged beyond those tiles with signals. To characterize FN rate, we inspected the tiles on the surface of the cluster of tiles having neuronal signals and counted the number of surface tiles with fluorescent signal on their surfaces. The FN rate is defined by the number of signal-containing outer surfaces divided by the total number of outer surfaces for the cluster with fluorescent signals (Figure 2G). Thus, FN rate reflected the number of outer surfaces with signals that were not detected. Typically, the FN rate was low, ~0.13%, corresponding to about 9 surfaces out of about 7000 surfaces (Figure 2H). One major contribution to FN rate was that signals from some neurons were relatively weak (accounting for over 96% of FN cases). Thus, there was on average only one undetected surface with bright signals in ~3 imaged brains (assuming 7000 surfaces in each brain, Figure 2I). As we only traced neurons with bright signals (neurons with weak signals were hard to trace), this tiny FN rate did not affect our pipeline of tracing. We also manually checked the completeness of traced individual neurons.

Image processing

Custom scripts were written in MATLAB (MathWorks) unless otherwise stated. Images acquired using 40x objective were used to interactively annotate single-neuron reconstructions, and images acquired using 16× objective were used for mapping the imaged brain to the Allen Mouse Common Coordinate Framework (CCFv3) (Wang et al., 2020). A global coordinate system was defined by the absolute stage positions of both the 40x and 16x tiles, so that any voxel in the 40x image volume can be mapped back onto the 16x image volume, and vice versa.

Image tiles acquired at 40x were grouped to their neighboring tiles if they were connected, resulting in a few groups of tiles with one major group having the majority of tiles (~90%). Other groups of tiles were disconnected from the major group, containing only a small number of tiles without fluorescent signals, and thus were abandoned for further analysis (Figure 2H). Then tiles in the major group were assembled into a large 3D image stack according to their positions recorded by stages during imaging, with the tile having smallest X and Y coordinates placed as the origin set. Signal mismatch occurred between tiles along the X, Y and Z axes. The mismatch along the X or Y axis was typically small, and was corrected by rigid transformation. The vertical mismatch along the z axis was corrected in Elastix (Klein et al., 2010). After registration, the large 3D image volume was saved as horizontal 2D tiff series along the z axis, with zeros filling in the non-imaged brain volume. Filling the non-imaged area with zeros was necessary to use standard software such as teraConverter to convert the full resolution whole-brain imaging data to a multiresolution format to enable visualization using Vaa3D (see annotation and visualization section).

Images acquired at 16x was stitched and registered using the same pipeline as above. The generated 16x whole-brain volume was down-sampled to 25 μm^3 voxel size in order to match the 25 μm scale of the Allen brain template. Then the 3D volume was registered to the Allen Mouse Common Coordinate Framework (CCFv3) by ANTs (Tustison et al., 2014). A global coordinate system was defined by the absolute stage positions of both the 40x and 16x tiles, so that any voxel in the 40x image volume can be mapped back on to the 16X image volume, and vice versa. Using this way, the 3D volume acquired using the 40x objective was registered to the CCF.

QUANTIFICATION AND STATISTICAL ANALYSIS

Annotation and visualization

Manual annotation of single neurons was performed using Vaa3d (Peng et al., 2010). The multiresolution whole-brain volume was imported to Vaa3d TeraFly plug-in which enabled visualization of any partial volume centered at a given position of interest at any selected resolution (Peng et al., 2014a). We typically chose a few brightest labeled neurons for annotation. Multiple annotators cooperated to trace the full morphology of single neurons. The first annotator started from the soma and drew each and every process of the neuron by mouse clicking and dragging, using the virtual finger function of Vaa3d which enabled accurate reconstruction of neuronal processes (Peng et al., 2014b). A second annotator checked the uncertain areas marked by the first annotator, and gave correction feedbacks to the first annotator. Finally, a third annotator, who typically had more experience in tracing of neuronal morphology, was introduced if there were any unresolved structure left, and made a final decision after discussion with the first two annotators. The resulting reconstruction of a single-neuron was saved in SWC format. Because projection neurons typically have processes with total length in several hundred millimeters and we accurately traced fine axonal collaterals using the virtual finger function of Vaa3D, each neuron on average requires about one week of full time work for annotation (the first annotator), with additional time for further checking.

For visualization and morphological analysis, SWC files generated from the annotation based on the 40x image volume were first mapped back to the 16x image volume through the global coordinate system. Then the same transformation as used in the 16x image volume was applied to the SWC files to map the coordinates to the CCF. The registered SWC files were used to visualize single neuron skeleton in the model mouse brain (Figure S2).

Statistics

Statistical details including the definitions and exact value of n (e.g., number of samples), p values, and the types of the statistical tests can be found in the figures and figure legends. All statistical tests were two-tailed, and the significance was assigned at $p < 0.05$.